



Title	Characteristics of Electron Conduction in a Gas under a Quadrupole Magnetic Field and Radio-Frequency Electric Fields
Author(s)	Sugawara, Hirotake
Citation	Japanese Journal of Applied Physics, 52, 056101 https://doi.org/10.7567/JJAP.52.056101
Issue Date	2013-05
Doc URL	http://hdl.handle.net/2115/53390
Rights	© 2013 The Japan Society of Applied Physics
Type	article (author version)
File Information	Sugawara-2013-JJAP-HUSCAP.pdf



[Instructions for use](#)

Characteristics of Electron Conduction in a Gas under a Quadrupole Magnetic Field and Radio-Frequency Electric Fields *

Hirotake SUGAWARA[†]

Graduate School of Information Science and Technology, Hokkaido University, Sapporo 060-0814, Japan

Electron conduction in CF_4 under a simplified model quadrupole magnetic field (QMF) and rf electric fields at $f = 13.56, 27.12,$ and 40.68 MHz was analyzed using a Monte Carlo method, following the manner of electron swarm analyses. This field configuration simulated current paths of magnetic neutral loop discharge plasmas used for dry etching. The electron conduction therein was focused on as an elemental process of plasma power deposition. The electrons formed a star-shaped distribution with four rays along the separatrices of the QMF. The effective electron conductivity quantified as the amplitude of mean electron velocity was high around the central axis. The time-averaged mean electron velocities in the four regions of the QMF were biased under a rectification effect of the magnetic field. With increasing f , the high-conductivity region expanded and ionization was promoted. An enhancement of plasma power deposition under high driving frequencies was indicated.

KEYWORDS: electron swarm, electron transport, Monte Carlo simulation, quadrupole magnetic field, NLD plasma

1. Introduction

A magnetic field is often applied to plasmas typically to confine or guide charged particles or to utilize the electron cyclotron resonance (ECR) for an efficient energy supply. The quadrupole magnetic field (QMF), focused on in this work, is specific for magnetic neutral loop discharge (NLD) plasmas, which are ring-shaped inductively coupled plasmas used for material processing.^{1–3} The QMF formed by three coaxial coils has a ring of zero magnetic field called a neutral loop (NL) and its strength increases with distance from the NL (see Fig. 1). Electrons can gain energy from an rf electric field, typically at 13.56 MHz, induced along the NL by an rf antenna mainly under a weak magnetic field near the NL. The NLD plasma, which is desirable for anisotropic etching, can be driven at low pressures of approximately 0.1–1.0 Pa.^{4–6} Although the NLD plasma is nonuniform, a modulation of the middle coil current to vary the NL radius flattened the etching rate profile on the substrate,⁷ and computational attempts to compose uniform ensembles of ion flux distributions on the substrate with weights of ion irradiation time at different NL radii and heights were also presented.^{8,9}

*Published source: Japanese Journal of Applied Physics **52**(5) 056101 (5 pages) (2013) May/2013, DOI: 10.7567/JJAP.52.056101

[†]E-mail: sugawara@ist.hokudai.ac.jp

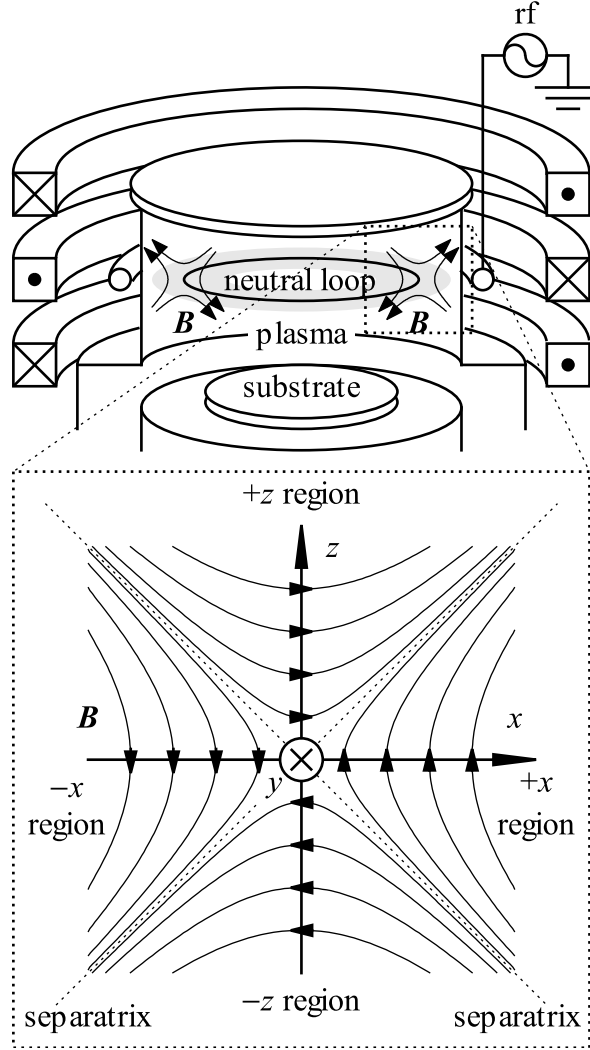


Fig. 1. Schematic of an NLD plasma reactor and model of QMF around the NL. The test magnetic field is defined as $\mathbf{B} = (B_x, B_y, B_z) = (\beta z, 0, \beta x)$, where $\beta = dB_x/dz = dB_z/dx$ is a positive constant. The electric field is applied as $\mathbf{E} = (E_x, E_y, E_z) = (0, E_0 \sin 2\pi ft, 0)$.

The electron conduction along the NL is a key factor governing the sustainment of plasma and the production of reactive species through plasma power deposition. In an equivalent circuit analysis to estimate the plasma power from the antenna voltage, the NLD plasma was treated as a simple ring conductor inductively coupled with an rf antenna.¹⁰ On the other hand, from a microscopic view, complex electron behaviors, such as chaotic electron meandering^{2, 11} and directional electron drift,^{12, 13} have been revealed by simulations in antiparallel gradient magnetic fields, a more simplified model than the QMF. The electron motion in QMFs has also been analyzed.^{8, 14–17} However, detailed structures and features of the electron conduction path in the QMF are still left unclarified.

In this study, the electron conduction in a model QMF is simulated using a Monte Carlo

method. The electron conduction path under the QMF is newly characterized in terms of electron distribution, energy gain, and drift velocity, or in other words, from the viewpoint of the response of a group of electrons. Furthermore, the dependence of the electron conduction in the QMF on the electric field frequency is investigated by comparing simulation results obtained at 13.56, 27.12, and 40.68 MHz.

2. Simulation Model and Conditions

2.1 Electric and magnetic fields

The model electric and magnetic fields (the \mathbf{E} and \mathbf{B} fields) were defined in a boundary-free space with rectangular coordinates (x, y, z) as

$$\mathbf{E} = (E_x, E_y, E_z) = (0, E_0 \sin 2\pi ft, 0), \quad (1)$$

$$\mathbf{B} = (B_x, B_y, B_z) = (\beta z, 0, \beta x), \quad (2)$$

where $\beta = dB_x/dz = dB_z/dx$. The modelled region in the reactor geometry is shown in Fig. 1. The NL has been opened into a straight line corresponding to the y -axis, as performed in preceding simulations.¹⁴⁻¹⁶ The \mathbf{E} field was treated to be uniform all over the model space and the effect of space charge was neglected, following the manner of electron swarm analyses. The strength of magnetic field around the NL was locally linear in a measurement^{18,19} and a calculation.²⁰ Although the QMF of a practical NLD plasma has nonlinear profiles in regions distant from the center and is asymmetric because of the curvature of the NL, β was assumed to be constant to recognize essential features of the electron conduction in the QMF. This \mathbf{B} field consists of two pairs of antiparallel gradient magnetic fields. Such magnetic fields can be formed by parallel-plane sheet currents.^{2,12}

The parameters used to determine the \mathbf{E} and \mathbf{B} fields were chosen to be $E_0 = -10.0 \text{ V cm}^{-1}$ and $\beta = 0.5 \text{ mT cm}^{-1}$ following an experimental condition.²¹ The driving frequency f was set at $f_1 = 13.56 \text{ MHz}$, $f_2 = 2f_1 = 27.12 \text{ MHz}$, and $f_3 = 3f_1 = 40.68 \text{ MHz}$. These are center frequencies of representative industry-science-medical rf bands.

Here, let us name the four regions of the \mathbf{B} field divided by the separatrices $z = \pm x$ as the $+x$ region ($z < x$ and $z > -x$), the $-x$ region ($z > x$ and $z < -x$), the $+z$ region ($z > x$ and $z > -x$), and the $-z$ region ($z < x$ and $z < -x$), as shown in Fig. 1. The antiparallel gradient magnetic fields composing the \mathbf{B} field are known to have a rectification effect on the electron flux along the y -axis.^{12,13} The direction of the rectification in each of the four regions is that of $\mathbf{B} \times \nabla|\mathbf{B}|$, i.e., the $+y$ direction in the $\pm x$ regions and the $-y$ direction in the $\pm z$ regions. Let us call this direction the forward direction hereafter and the opposite is the reversed direction.

2.2 Monte Carlo simulation

The electron motion in the \mathbf{E} and \mathbf{B} fields was simulated using a Monte Carlo method. The initial electrons were released from the origin with velocities chosen at random from a Maxwellian distribution with a mean energy of 1 eV. The electron trajectory described with the motion equations $d\mathbf{v}/dt = -(e/m)(\mathbf{E} + \mathbf{v} \times \mathbf{B})$ and $d\mathbf{r}/dt = \mathbf{v}$ was calculated for 100 rf periods using the Runge–Kutta method, where $\mathbf{r} = (x, y, z)$ and $\mathbf{v} = (v_x, v_y, v_z)$ are the electron position and velocity, and e and m are the electronic charge and mass, respectively. The simulation time step was set at a sufficiently short value of 3.07 ps, which was 1/24000, 1/12000, and 1/8000 of the rf periods at f_1 , f_2 , and f_3 , respectively.

The ambient gas was assumed to be CF_4 . The number density of gas molecules was set at $1.77 \times 10^{14} \text{ cm}^{-3}$ (0.67 Pa at 0 °C). The electron collision cross sections of CF_4 were obtained from Ref. 22. A time-saving judgment scheme for electron–molecule collisions²³ was adopted.

More than 1×10^6 electrons were sampled to obtain the spatial electron distribution and other quantities after 90 rf periods, by which the mean electron energy and the average electron velocity had reached their periodical steady states.

3. Results and Discussion

3.1 Single electron motion

Figure 2 shows an example of an electron locus under the \mathbf{B} and \mathbf{E} fields at f_1 . Two fundamental motions were included in an electron flight between two successive collisional scatterings. One was meandering near and along the y -axis under a weak magnetic field, where the electron gained energy from the \mathbf{E} field. The other was gyration under a strong magnetic field away from the y -axis, where the energy gain was small. The electron moved along the separatrices when gyrating away from the y -axis. Magnetic field lines approaching the separatrices guided the electron.

The electron underwent two subsequent motions during gyration. One was a reciprocating motion along magnetic field lines due to the magnetic mirror effect. The electron moved away from the y -axis and turned back after reflection by the magnetic mirror. The electron tended to remain in one of the four regions during this process. The other was the grad- B drift toward the reversed direction in each of the four regions. This drift split the y distributions of electrons between the $\pm x$ and $\pm z$ regions as shown later.

The electron transferred between neighboring two of the four regions primarily during meandering near the y -axis. This inter-regional electron transfer tended to originate from the regions in which the electron acceleration by the \mathbf{E} field was in the forward direction to those in which the acceleration was in the reversed direction, e.g., from the $\pm x$ regions to the $\pm z$ regions during the former half of an rf period. This was because the Lorentz force let the electrons flying in the forward direction turn inward in the former regions and outward in the latter regions. As a result, the electron populations in the $\pm x$ and $\pm z$ regions increased and

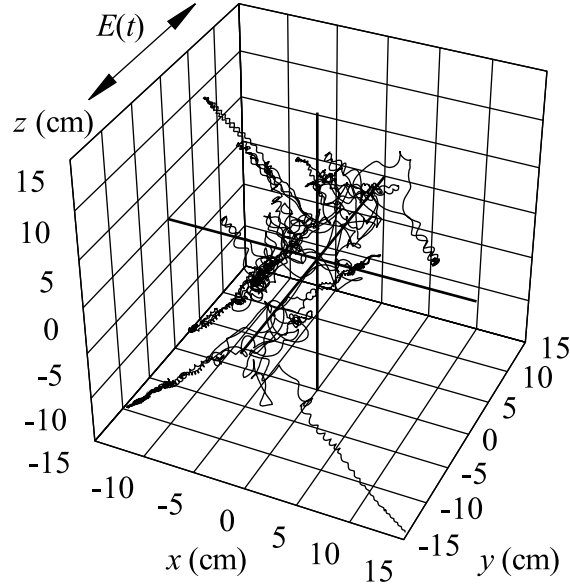


Fig. 2. Example of locus of single electron motion in the quadrupole \mathbf{B} field and the rf \mathbf{E} field at f_1 .

decreased complementarily and alternatingly every half an rf period.

3.2 Electron distribution

Figure 3 shows the electron distribution $N_e(x, z)$ under the \mathbf{B} and \mathbf{E} fields at f_1 . This is a cross section of the electron conduction path. The electron position was projected to the xz -plane and $N_e(x, z)$ has been normalized to satisfy $\int_{-\infty}^{\infty} \int_{-\infty}^{\infty} N_e(x, z) dx dz = 1$.

The four rays of the star-shaped distribution were formed by the action of the magnetic field lines to guide electrons along the separatrices as seen in Fig. 2. The center dip of $N_e(x, z)$ was formed because the electrons that accelerated near the y -axis were likely to deviate from it.

3.3 Energy gain and electron multiplication

Figure 4 shows the normalized distribution of net electron energy gain $G(x, z)$ at f_1 . $G(x, z)$ consists of the terms of the energy gain and loss due to acceleration and deceleration by the \mathbf{E} field, respectively, and the energy loss by inelastic collisions. $G(x, z)$ has been normalized so that $\int_{-\infty}^{\infty} \int_{-\infty}^{\infty} G(x, z) dx dz$ gives the energy gain in eV per electron per rf period.

Positive values of $G(x, z)$ around the center confirm a conventional understanding that the electron energy gain occurs under a weak magnetic field. The energy gain is high even though $N_e(x, z)$ has a dip there. On the other hand, negative values of $G(x, z)$ along the separatrices indicate that the energy deposited to electrons around the center is transported along the separatrices and consumed there.

The electron energy gain correlated with the amplitude $A(x, z)$ of the y component $\bar{v}_y(x, z, t)$ of local mean electron velocity. The waveforms of $\bar{v}_y(x, z, t)$ were approximately

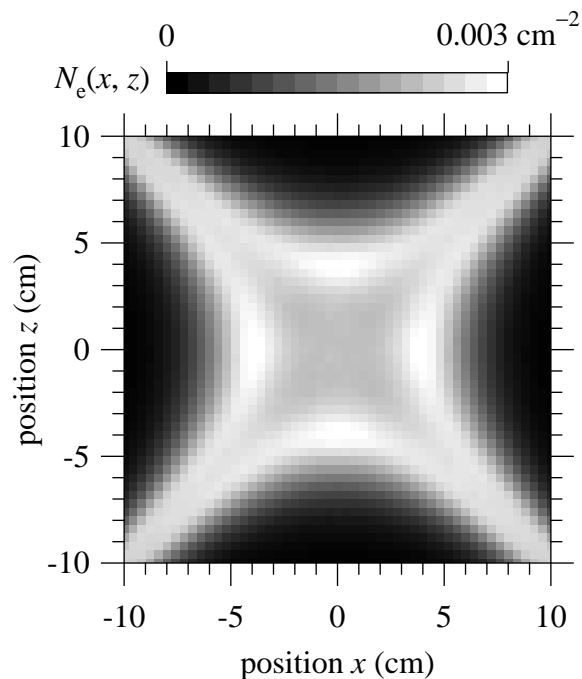


Fig. 3. Electron distribution $N_e(x, z)$ in the quadrupole \mathbf{B} field and the rf \mathbf{E} field at f_1 . See also Fig. 11 for values of $N_e(x, z = 0)$.

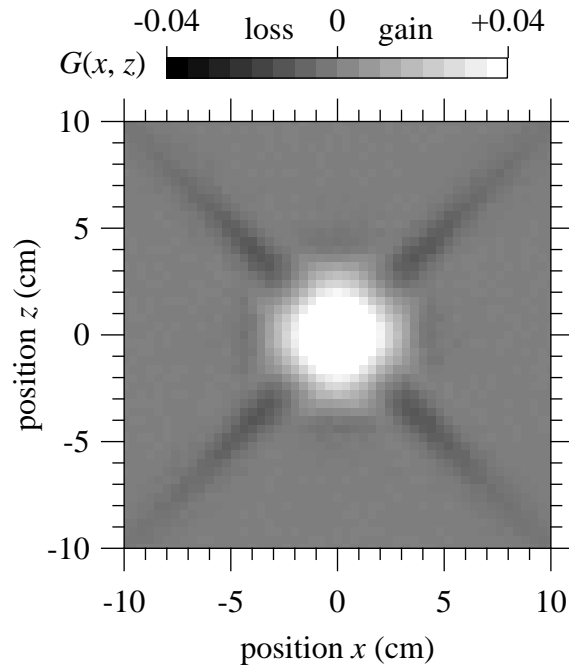


Fig. 4. Position-dependent net electron energy gain $G(x, z)$ at f_1 . $G(x, z)$ includes the gain by acceleration, the loss by deceleration, and the loss by inelastic collisions. The values of $G(x, z)$ are in such a unit that $\int_{-\infty}^{\infty} \int_{-\infty}^{\infty} G(x, z) dx dz$ gives the energy gain in eV per electron per rf period.

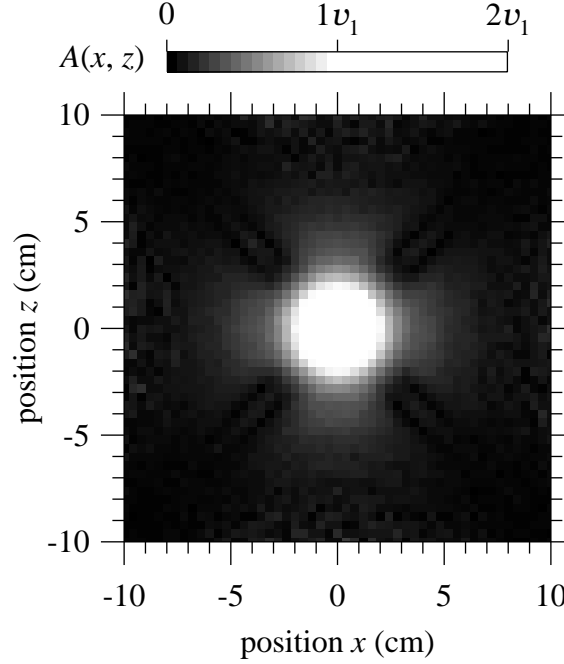


Fig. 5. Position-dependent amplitude $A(x, z)$ of mean electron velocity $\bar{v}_y(x, z, t)$ at f_1 . v_1 is the electron speed associated with 1 eV. See also Fig. 10 for values of $A(x, z = 0)$.

sinusoidal. Then, $A(x, z)$ was obtained by the least-squares fitting assuming the following:

$$\bar{v}_y(x, z, t) = a(x, z) \sin 2\pi ft + b(x, z) \cos 2\pi ft + c(x, z), \quad (3)$$

$$A(x, z) = \sqrt{[a(x, z)]^2 + [b(x, z)]^2}, \quad (4)$$

where a , b , and c are the fitting parameters. The effective electron mobility would be estimated from $A(x, z)/|E_0|$. $A(x, z)$ shown in Fig. 5 peaked at the center similarly to $G(x, z)$. High $A(x, z)$ values indicate a sensitive electron response to the \mathbf{E} field and a commensurately high energy gain.

Figure 6 shows the normalized ionization rate $I(x, z)$. This is a quantification of representative energy consumption. $\int_{-\infty}^{\infty} \int_{-\infty}^{\infty} I(x, z) dx dz$ gives the number of ionization collisions per electron per rf period. The four-rayed star-shaped $I(x, z)$ agrees with the interpretation on the energy transport along the separatrices.

3.4 Directionality of the electron flow

Figure 7 shows the time-averaged y component $W_y(x, z)$ of $\bar{v}_y(x, z, t)$, i.e., the dc bias $c(x, z)$. The structure of counter electron fluxes toward the $\pm y$ directions is observed clearly. The mechanism of forming this directionality and the reversed part around the center was explained in detail in Ref. 13 on the basis of the local directionality of electron motion in gyro-trajectory.

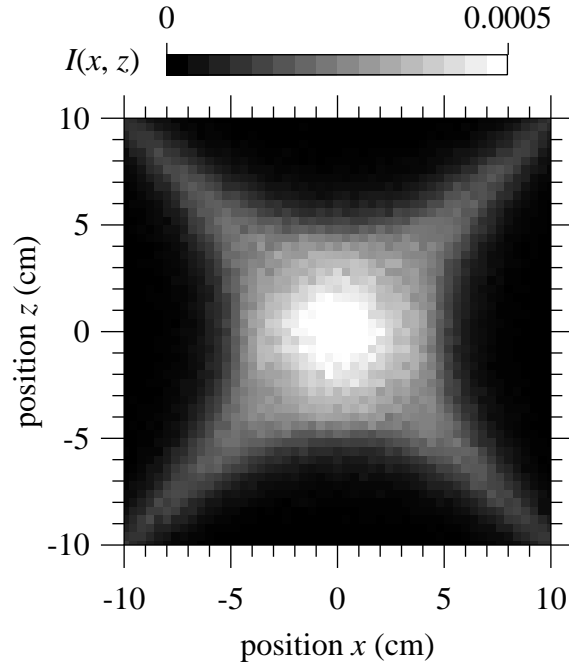


Fig. 6. Time-averaged ionization rate $I(x, z)$ at f_1 . The values of $I(x, z)$ are in such a unit that $\int_{-\infty}^{\infty} \int_{-\infty}^{\infty} I(x, z) dx dz$ gives the number of ionization collisions per electron per rf period.

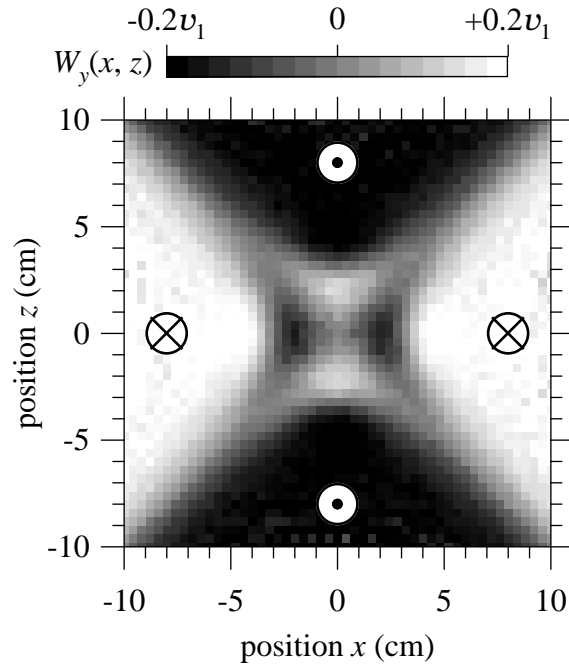


Fig. 7. Position-dependent time-averaged y component $W_y(x, z)$ of electron drift velocity at f_1 . v_1 is the electron speed associated with 1 eV. See also Fig. 12 for values of $W_y(x, z = 0)$. The forward direction, i.e., that of $\mathbf{B} \times \nabla|\mathbf{B}|$, in each of the $\pm x$ and $\pm z$ regions is indicated in the figure.

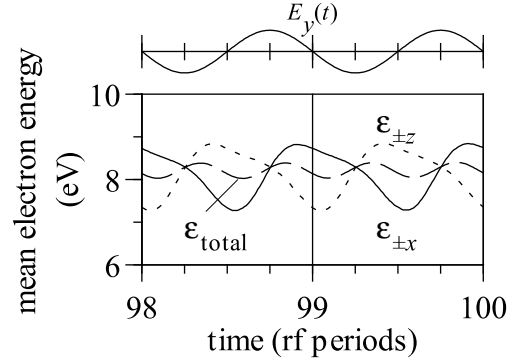


Fig. 8. Temporal variations in mean electron energies in the $\pm x$ and $\pm z$ regions.

These opposite directionalities induced a complementary response of electrons between the $\pm x$ and $\pm z$ regions. Figure 8 shows temporal variations in the mean energies $\varepsilon_{\pm x}$ and $\varepsilon_{\pm z}$ of the electrons in the $\pm x$ and $\pm z$ regions, respectively, and the $\varepsilon_{\text{total}}$ of all electrons. $\varepsilon_{\pm x}$ and $\varepsilon_{\pm z}$ had a phase difference of π . $\varepsilon_{\pm z}$ increased in the former half of an rf period because the electrons that accelerated near the y -axis transferred from the $\pm x$ regions to the $\pm z$ regions with heightened energies. The variation in the latter half was opposite.

Figure 9 shows the y positions of the centers of mass, $g_{\pm x}$ and $g_{\pm z}$, of electrons in the $\pm x$ and $\pm z$ regions, respectively, and the g_{total} of all electrons. The grad- B drifts toward the opposite directions in the $\pm x$ and $\pm z$ regions separated $g_{\pm x}$ and $g_{\pm z}$. Here, the direction of the grad- B drift is known to be opposite to that of the time-averaged electron flux,¹³ and the early shift in $g_{\pm x}$, $g_{\pm z}$, and g_{total} toward the $+y$ direction was simply due to the initial phase of the \mathbf{E} field. The separation between $g_{\pm x}$ and $g_{\pm z}$ saturated at a distance d because the inter-regional electron transfer between the $\pm x$ and $\pm z$ regions suppressed further separation. The shifts in $g_{\pm x}$ and $g_{\pm z}$ correspond to clockwise and anticlockwise rotational displacements of electrons if in a loop current path as is in an NLD plasma. These loop currents are the counterpart of the rf antenna in inductive coupling. The relation $\nu d = \bar{W}_y$ is derived from a moment balance in equilibrium, where ν is the frequency of inter-regional transfer and \bar{W}_y is the average drift velocity in each of the $\pm x$ and $\pm z$ regions. The separation d represents the average electron displacement in y between two successive inter-regional transfers.

3.5 Driving frequency dependence

Figures 10 and 11 show $A(x, z)$ and $N_e(x, z)$, respectively, on the x -axis at $f = f_1, f_2$, and f_3 .

The breadth of $A(x, z)$ represents the effective thickness of the electron conduction path. It was less than the breadth of $N_e(x, z)$ at f_1 , but increased with f . This increase was caused most likely by the expansion of the electron meandering region. The positions $x_i = 4\pi f_i m / (e\beta)$

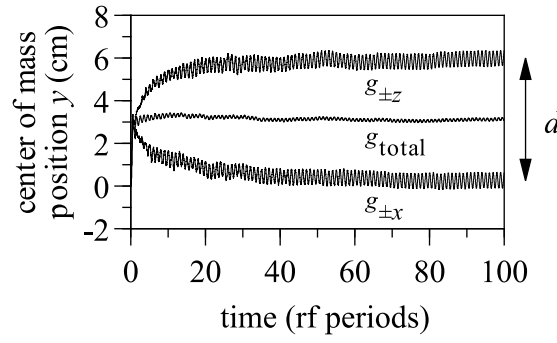


Fig. 9. Temporal variations in the y positions of centers of mass of electrons in the $\pm x$ and $\pm z$ regions.

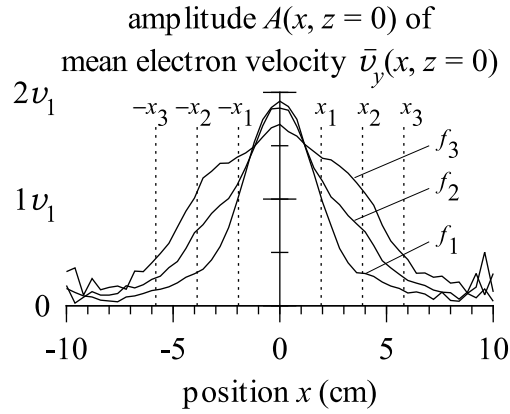


Fig. 10. Comparison of amplitudes $A(x, z)$ of mean electron velocity $\bar{v}_y(x, z, t)$ on the x -axis at f_1 , f_2 , and f_3 . The fluctuation in the regions away from the center was due to small electron populations there. $x_i = 4\pi f_i m / (e\beta)$ ($i = 1, 2$, and 3) are the positions at which $|\mathbf{B}| = 2B_{\text{ECR}}$, where $B_{\text{ECR}} = 2\pi f(m/e)$ is the rf-resonant magnetic field strength.

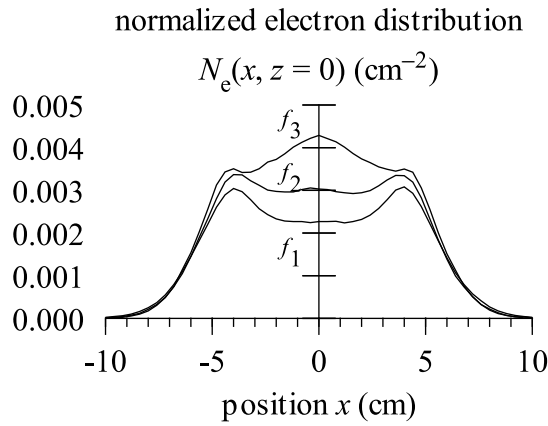


Fig. 11. Comparison of electron distributions $N_e(x, z)$ on the x -axis at f_1 , f_2 , and f_3 .

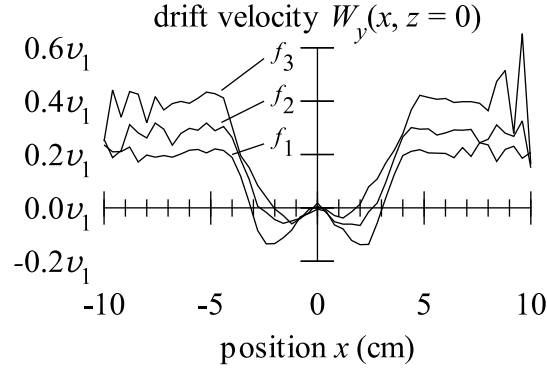


Fig. 12. Comparison of $W_y(x, z)$ values on the x -axis at f_1 , f_2 , and f_3 . v_1 is the electron speed associated with 1 eV.

($i = 1, 2$, and 3) satisfying $|\mathbf{B}| = 2B_{\text{ECR}}$ are denoted by broken lines in Fig. 10. Here, $B_{\text{ECR}} = 2\pi f(m/e)$ is the rf-resonant magnetic field strength at which ECR occurs. The ECR position is often referred to as a measure used to estimate the width of electron meandering.^{2,15} Electrons tend to meander in the region of $|\mathbf{B}| < 2B_{\text{ECR}}$, while electrons can complete one or more cycles of gyration during an rf period in the region of $|\mathbf{B}| > 2B_{\text{ECR}}$.

Fundamental features of $N_e(x, z)$, such as the four-rayed star shape, the position of shoulders, and the decay of distribution tails in the cross section shown in Fig. 11, were almost unchanged irrespective of f . On the other hand, $N_e(x, z)$ around the center increased with f because of the enhancement of electron multiplication due to ionization. The widening of the electron conduction path with increasing f made the electron energy gain from the rf \mathbf{E} field easier.

When the space charge field is significant as in practical NLD plasmas, the positive ions produced around the y -axis would attract electrons inward. An increase in the number of electrons near the y -axis, which are susceptible to the rf \mathbf{E} field, would also promote the electron energy gain. This process was suggested on the basis of the results of an NLD plasma simulation considering Poisson's equation in an axisymmetrical geometry.²⁴ It is expected that the widening of the electron conduction path in an NLD plasma will contribute to the sustainment of the plasma in collaboration with the effect of the space charge field through the enhancement of the electric power deposition to the plasma.

Figures 12 and 13 respectively show the dependences of the time-averaged electron velocity $W_y(x, z)$ and flux $N_e(x, z)W_y(x, z)$ on f observed on the x -axis. Their profiles along the z -axis were of inverse signs. The forward and backward electron flows near the center cancelled each other, but a dc bias was left in the outer regions. The bias was enhanced by increasing f . The mechanism of inducing this enhancement is currently unclear.

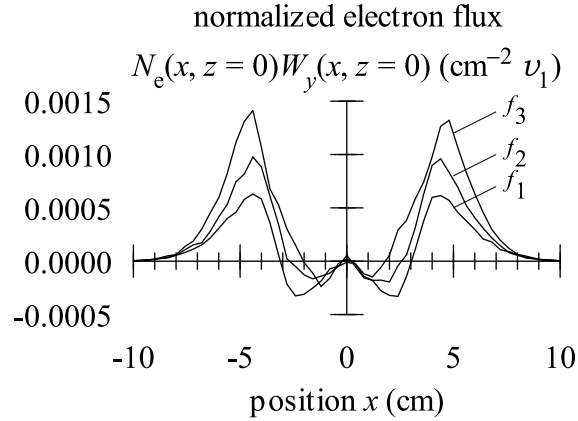


Fig. 13. Comparison of normalized electron fluxes $N_e(x, z)W_y(x, z)$ on the x -axis at f_1 , f_2 , and f_3 . v_1 is the electron speed associated with 1 eV.

4. Conclusions

The electron motion in a model QMF was simulated using a Monte Carlo method.

The electrons formed a four-rayed star-shaped distribution around the central axis of the electron conduction path. This was because the magnetic field lines approaching the four-way separatrices of the QMF guided the gyrating electrons. Electrons gained energy around the central axis and were transported along the separatrices. As a result, the production of ions, utilized as etchants, also distributed around the separatrices in addition to the central axis.

The electron conduction path under the QMF had a core compliant to the rf \mathbf{E} field and clad with directionalities. The directionalities were toward the direction of $\mathbf{B} \times \nabla|\mathbf{B}|$, which was opposite between the $\pm x$ and $\pm z$ regions. The thickness of the electron conduction path quantified as the amplitude of the mean electron velocity increased with rf \mathbf{E} field frequency. This was because the region of electron meandering allowing electron energy gain expanded.

Although the present analysis was performed in the most simplified model, the essential structure of the electron conduction path in the QMF was illustrated in detail. The obtained results indicate that the enhancement of electric power deposition, desirable for the sustainment of NLD plasmas and the promotion of etchant ion production, can be expected by adopting a high driving frequency.

Acknowledgments

This work was supported by a Grant-in-Aid for Scientific Research No. 22540500 from the Japan Society for the Promotion of Science and by ULVAC Inc. The author wishes to thank Dr Seiji Ogata, formerly of ULVAC, for stimulating discussions on electron mobility in nonuniform magnetic fields.

References

- 1) T. Uchida: Jpn. J. Appl. Phys. **33** (1994) L43.
- 2) T. Uchida: J. Vac. Sci. Technol. A **16** (1998) 1529.
- 3) T. Uchida and S. Hamaguchi: J. Phys. D **41** (2008) 083001.
- 4) H. Tsuboi, M. Itoh, M. Tanabe, T. Hayashi, and T. Uchida: Jpn. J. Appl. Phys. **34** (1995) 2476.
- 5) H. Tsuboi, T. Hayashi, and T. Uchida: Jpn. J. Appl. Phys. **36** (1997) 6540.
- 6) D. O'Connell, D. L. Crintea, T. Gans, and U. Czarnetzki: Plasma Sources Sci. Technol. **16** (2007) 543.
- 7) W. Chen, Y. Morikawa, M. Ito, T. Hayashi, K. Sugita, H. Shindo, and T. Uchida: J. Vac. Sci. Technol. A **17** (1999) 2546.
- 8) Y. Sakurai, T. Osaga, and H. Sugawara: IEEE Trans. Plasma Sci. **39** (2011) Pt. 1, 2550.
- 9) T. Yoshida, Y. Sakurai, H. Sugawara, and A. Murayama: Denki Gakkai Ronbunshi A **132** (2012) 278 [in Japanese]. To be translated into English for publication in Electr. Eng. Jpn.
- 10) H. Tsuboi and S. Ogata: Jpn. J. Appl. Phys. **46** (2007) 7475.
- 11) Z. Yoshida, H. Asakura, H. Kakuno, J. Morikawa, K. Takenuma, S. Takizawa, and T. Uchida: Phys. Rev. Lett. **81** (1998) 2458.
- 12) H. Sugawara and Y. Sakai: J. Phys. D **41** (2008) 135208.
- 13) H. Sugawara, T. Osaga, and H. Yamamoto: Plasma Sources Sci. Technol. **20** (2011) 055002.
- 14) H. Sugawara: Proc. 30th Int. Conf. Phenomena in Ionized Gases, 2011, A2-3.
- 15) Y. M. Sung, K. Uchino, and T. Sakoda: J. Vac. Sci. Technol. A **18** (2000) 2149.
- 16) T. Sakoda, Y. Okraku-Yirenkyi, Y.-M. Sung, M. Otsubo, and C. Honda: Jpn. J. Appl. Phys. **40** (2001) 6607.
- 17) T. Osaga, H. Sugawara, and Y. Sakurai: Plasma Sources Sci. Technol. **20** (2011) 065003.
- 18) T. Sakoda, H. Iwamiya, K. Uchino, K. Muraoka, M. Ito, and T. Uchida: Jpn. J. Appl. Phys. **36** (1997) L67.
- 19) T. Sakoda, T. Miyao, K. Uchino, and K. Muraoka: Jpn. J. Appl. Phys. **36** (1997b) 6981.
- 20) T. Gans, D. L. Crintea, D. O'Connell, and U. Czarnetzki: J. Phys. D **40** (2007) 4508.
- 21) H. Sugawara, T. Osaga, H. Tsuboi, K. Kuwahara, and S. Ogata: Jpn. J. Appl. Phys. **49** (2010) 086001.
- 22) M. Kurihara, Z. Lj. Petrović, and T. Makabe: J. Phys. D **33** (2000) 2146.
- 23) H. Sugawara, N. Mori, Y. Sakai, and Y. Suda: J. Comput. Phys. **223** (2007) 298.
- 24) Y. Sakurai, T. Yoshida, H. Sugawara, and A. Murayama: Proc. 2011 Annu. Conf. Fundam. Mater. Soc. IEEJ, 2011, XI-11 [in Japanese].